Rapid near-infrared diffuse tomography for hemodynamic imaging using a low-coherence wideband light source

Daqing Piao
Oklahoma State University
School of Electrical & Computer Engineering
Stillwater, Oklahoma 74078-5032
E-mail: daqing.piao@okstate.edu

Brian W. Pogue
Dartmouth College
Thayer School of Engineering
Hanover, New Hampshire 03755-8000

Abstract. Rapid near-infrared (NIR) diffuse optical tomography is implemented using a low-coherence source. The spectral bandwidth of the low-coherence source is dispersed and coupled to linearly bundled fibers, such that "spread"-spectral encoding among the bundled fibers is formed, and could be used for parallel source illumination onto tissue. In comparison with a previous spectral-encoding technique that employed multiple laser diodes, the use of a low-coherence source for spread-spectral encoding presents a few unique characteristics: (1) it provides shift-free spectral encoding; (2) it reduces the reconstruction uncertainty significantly owing to the minimization of spontaneous channel-to-channel intensity fluctuation; and (3) it enables the implementation of NIR tomography into an endoscopic imaging mode. A 20-mW superluminescent diode centered at 840 nm with a 40-nm bandwidth is used as the source, and a sampling speed of 5 Hz is obtained in a 27-mm imaging array consisting of eight sources and eight detection channels. The principles of using a low-coherence source for spread-spectral encoding are elaborated, the characteristic performances are demonstrated, and the preliminary results of imaging hemoglobin absorption variations during 10 s of voluntary breath-holding are presented. [DOI: 10.1117/1.2709636]

Keywords: biomedical optics; tomography; medical imaging.

Paper 06192R received Jul. 24, 2006; revised manuscript received Oct. 15, 2006; accepted for publication Oct. 16, 2006; published online Feb. 28, 2007.

1 Introduction

Near-infrared (NIR) diffuse optical tomography (DOT) is an interesting noninvasive imaging technique that provides blood-based functional contrast. The diagnostic premises of NIR-DOT have been demonstrated on the detection of breast cancer as well as the assessment of brain functionality.[1–12] NIR-DOT takes advantage of the high intrinsic optical absorption of hemoglobin as compared to other tissue constituents such as water in the NIR spectral region, which in principle enables high sensitivity and potentially rapid sampling for hemodynamic imaging applications. However, NIR imaging uses diffused photons as measured through transmission of significant volumes of tissue, and after they undergo many scattering events. Thus, the intrinsic information related to where the photon was launched from is lost when it is detected, and therefore a mechanism of differentiating the origin of the signal path from a particular source to a detector must be implemented. This is especially important for high imaging speed, where sequential illumination significantly decreases the illumination time. Simultaneous source-detector (S-D) pair separation through frequency encoding has been widely applied, however, the imaging speeds of such systems rarely surpassed 1 Hz for thick tissue tomographic imaging due to the extensive rf instrumentation required for frequency multiplexing and the detection of rf signals in many channels.[1,3,5] A sampling speed below 1 Hz is less likely to provide the dynamic physiological changes that are known to occur in the vascular space with changes in pulsation, blood pressure, contrast agent flow, or response to pressure. NIR tomography at 2- to 3-Hz frame rate has been demonstrated by mechanical switching of the source.[13,14] In this configuration, one laser diode (LD) is used for one "color" of the NIR tomography, and the LD output is sequentially coupled to each source channel by a fast scanning setup driven by a high-speed stepper motor. This frame rate can be significantly increased by decreasing the number of sequential sources used; however, this will also decrease the overall image quality proportionately. The use of switching is certainly the most straightforward method for the isolation of S-D channels; however, it does not necessarily reach the highest speed due to the sequential switching where a start-stop scanning pattern is necessary to have sufficient illumination in each channel for a detectable signal-to-noise ratio (SNR). The use of mechanical switching may also degrade the system's stability and perfor-

Address all correspondence to Daqing Piao, Electrical & Computer Engineering, Oklahoma State University, 202 Engineering South, Stillwater, OK 74078-5032; Tel: 405-744-5250; Fax: 405-744-9198; E-mail: daqing.piao@okstate.edu

1083-3668/2007/12(1)/014016/12/$25.00 © 2007 SPIE

mance in the long term due to environmental factors such as vibration.

Rapid NIR tomography up to video-rate sampling was demonstrated by spectral encoding of multiple LDs in our previous work.[15,16] In this approach, each LD is operated at a unique wavelength, and many LDs provide a series of emissions that are spectrally encoded. This source spectral encoding ensures parallel illumination of all source channels and parallel decoding of all S-D signals by spectrometer separation. Simultaneous sampling of all S-D pairs is therefore feasible with data acquisition devices such as a CCD camera. Imaging speeds up to 35 Hz have been achieved based on this technique, which enables real-time imaging of fast hemodynamic responses in small animals.[17] This LD-based spectral-encoding technique, however, is subject to a few limitations. In this LD-based spectral-encoding configuration, a separate constant-current driver and a temperature controller are required for each LD to tune the emission wavelength precisely and independently. When many LDs are implemented, the wavelength difference in between neighboring channels must be maintained at a very small number ($\sim$1 nm) such that the overall spectral band of the sources does not introduce significant wavelength-dependent absorption variance among the source channels. This requires that the emission wavelength of each LD be maintained at high accuracy. This, however, becomes problematic if mode-hopping occurs among the LDs. Moreover, since each LD is driven separately, the light intensity variations among the channels are noncorrelated. The spontaneous intensity fluctuation among channels could affect the data calibration, thereby degrading the uncertainty of the imaging due to the ill-conditioning of NIR tomography reconstruction. It has been found in this LD-based spectral-encoding system that an overall intensity fluctuation of 1.2% occurs over a 30-min period, which causes an uncertainty of 4.8% in the reconstructed absorption coefficient. In this LD-based system, a reference channel was deployed to monitor the intensity fluctuation and the wavelength shift of each LD. This setup might be useful to compensate for the detected intensity fluctuation with respect to an original reference; nevertheless, when there is a spectral band overlapping or crossing due to spontaneous LD mode-hopping, the spectral-encoding profile is altered, the complete S-D signal pairs could not be discerned, and the data may have to be discarded.

In this paper, we present an alternative configuration of spectral encoding for rapid sampling of biological tissues in NIR tomography. This alternative approach utilizes a single low-coherence source instead of multiple LDs, and bundled fibers instead of individual fiber patch cords used for LD coupling. The spectrum of the low-coherence (or equivalently wideband) light source is dispersed by a grating, and coupled unto linearly bundled fibers. Such a configuration forms a spread-spectral encoding among the bundled fibers, in which the spectral encoding is free of alteration, and the fluctuation among encoding intensities is minimized. Moreover, this configuration enables the arrangement of the fiber arrays in an endoscopic outward-imaging geometry that extends rapid NIR tomography to imaging of internal organs.[18] A 20-mW superluminescent diode centered at 840 nm with a 40-nm bandwidth is used for the spread-spectral-encoding configuration, and a 5-Hz imaging rate is achieved by a 27-mm imaging array consisting eight sources and eight detectors. In this paper, the design that underlines this technique is introduced, the performance and calibration of this system are presented, and the imaging of periodical absorption changes induced by hemodynamic variations are demonstrated *in vivo*.

2 Principle of Spectral Encoding Using a Low-Coherence Source

2.1 *Review of Spectral Encoding Based on Multiple Laser Diodes*

NIR tomography measurement of discriminated S-D signals can be described intuitively by the following equation:

$$\begin{bmatrix}\text{signals for}\\ \text{all S-D pairs}\end{bmatrix} = \begin{bmatrix}\text{detector}\\ \text{decoding}\end{bmatrix}\begin{bmatrix}\text{sensitivity}\\ \text{matrix}\end{bmatrix}\begin{bmatrix}\text{source}\\ \text{encoding}\end{bmatrix} \times [\text{sources}], \quad (1)$$

and for each detector, the measurement M corresponds to a total of N sources as specified by the following matrix formulation of Eq. (1):

$$\mathbf{M}_{N\times 1} = \mathbf{\Gamma}^{-1}_{N\times N}\mathbf{W}_{N\times N}\mathbf{\Gamma}_{N\times N}\mathbf{S}_{N\times 1}, \quad (2)$$

where $\mathbf{S}$ denotes the source, $\mathbf{\Gamma}$ represents the encoding operation applied to the source, $\mathbf{W}$ accounts for the weight matrix or sensitivity matrix that is determined by the optical properties of the medium as well as the geometry of the imaging array, and $\mathbf{\Gamma}^{-1}$ indicates the decoding operation applied to the detector.

When the source encoding is performed by sequential switching,[13] the encoding and decoding operations are time-based such that they can be expressed as $\mathbf{\Gamma}(t)$ and $\mathbf{\Gamma}^{-1}(t)$. This configuration provides the most straightforward encoding; however, the time-series multiplexing may ultimately limit the imaging speed. Parallel launching of the sources can improve the imaging speed in principle, whereby a source-encoding mechanism, other than a time-based operation, is necessary. Frequency multiplexing is a commonly used method for parallel source illumination, where the encoding and decoding operators become frequency based, as described by $\mathbf{\Gamma}(f)$ and $\mathbf{\Gamma}^{-1}(f)$. In frequency multiplexing although the S-D pairs can be sampled simultaneously, the detectable dynamic range of each S-D signal is linearly reduced when more sources are added on, and the lowest level signals are potentially buried under the noise present in the higher intensity signals.

A potentially more robust approach of parallel source illumination is the spectral-encoding technique.[15,16] Multiple LDs are used in this configuration as in frequency multiplexing, whereas the source encoding is performed by spectral discrimination that is to operate each LD at different wavelength. Correspondingly the decoding of the signal is obtained by spectroscopic separation, as illustrated in Fig. 1(a). The encoding/decoding operations in this configuration are wavelength based as expressed by $\mathbf{\Gamma}(\lambda)$ and $\mathbf{\Gamma}^{-1}(\lambda)$, and Eq. (2) can be specified as

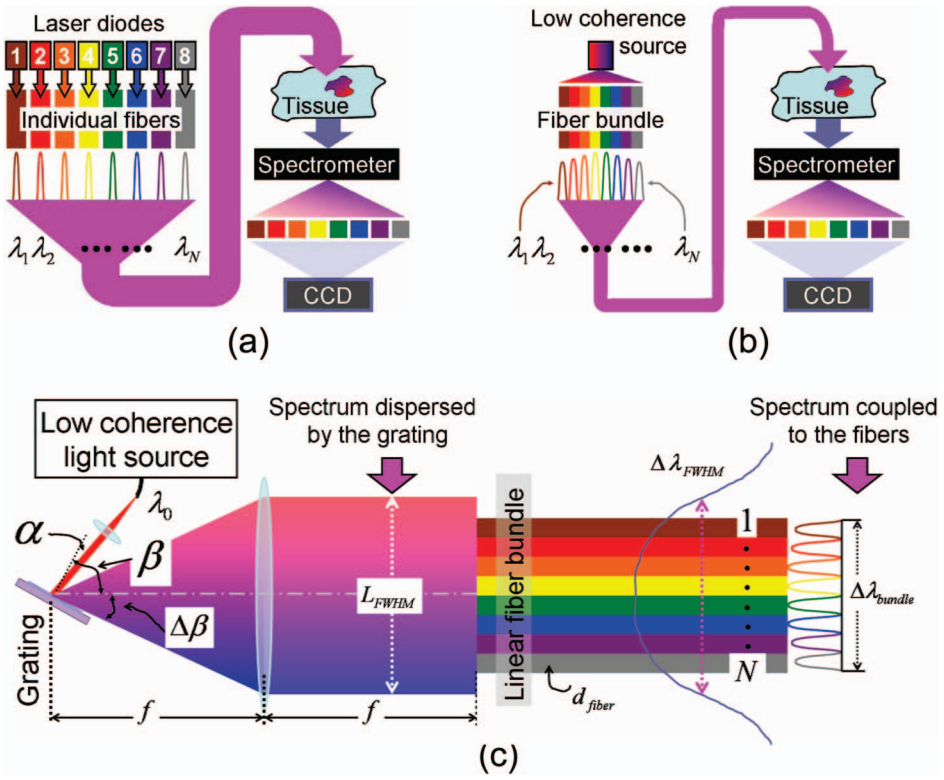

Fig. 1 (a) Spectral encoding based on multiple LDs shown schematically, (b) the spread-spectral encoding based on a low-coherence source, and in (c) details of a spread-spectral encoding illustrated from the source into the fibers, prior to the tissue.

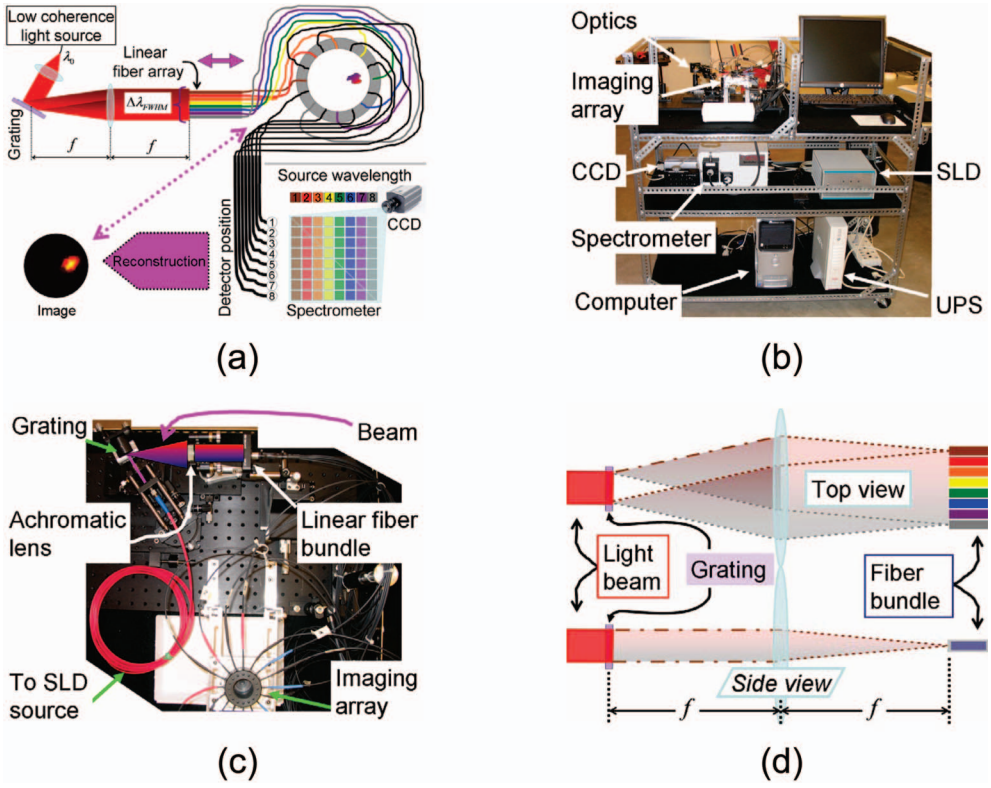

Fig. 3 (a) Schematic diagram of the spread-spectral-encoding system, (b) photograph of the system, (c) photograph of the spread-spectral-encoding optics, and (d) a detailed view of the coupling of the dispersed beam over to the linearly bundled fibers.

$$\begin{bmatrix} M_1 \\ M_2 \\ \vdots \\ M_N \end{bmatrix} = \begin{bmatrix} 1/\langle\lambda_1\rangle & 0 & \dots & 0 \\ 0 & 1/\langle\lambda_2\rangle & \dots & 0 \\ \vdots & \vdots & \dots & \vdots \\ 0 & 0 & \dots & 1/\langle\lambda_N\rangle \end{bmatrix} \times \begin{bmatrix} W_{11} & 0 & \dots & 0 \\ 0 & W_{22} & \dots & 0 \\ \vdots & \vdots & \dots & \vdots \\ 0 & 0 & \dots & W_{NN} \end{bmatrix} \begin{bmatrix} \langle\lambda_1\rangle & 0 & \dots & 0 \\ 0 & \langle\lambda_2\rangle & \dots & 0 \\ \vdots & \vdots & \dots & \vdots \\ 0 & 0 & \dots & \langle\lambda_N\rangle \end{bmatrix} \times \begin{bmatrix} S_1 \\ S_2 \\ \vdots \\ S_N \end{bmatrix}, \quad (3)$$

where $\langle\lambda_n\rangle$ $(n=1,2,\dots,N)$ indicates that a wavelength of λ_n is chosen for the source, and $1/\langle\lambda_n\rangle$ represents that the signal is separated with respect to λ_n. In the weight matrix $\mathbf{W}_{mn}$ $(m,n=1,2,\dots,N)$, the index m denotes the encoding wavelength chosen for the source, and the index n identifies the source contributing to the measured tissue volume. This approach performs the decoding of all S-D pairs prior to the photoelectronic conversion for signal sampling; thereby, in principle, a higher sampling speed can be reached without compromising the dynamic range of each S-D channel.[16]

2.2 *Spread-Spectral Encoding Based on a Low-Coherence Source*

In this work, an alternative spectral-encoding configuration is implemented. This technology, specified as "spread-spectral encoding," is based on a low-coherence (implying a wide bandwidth) light source rather than multiple LDs. The methodology of this approach is illustrated in Figs. 1(b) and 1(c). The spectrum of a low-coherence source can be dispersed by a grating and collimated thereafter to form a 1-D spatial spectral distribution. This linear spectral distribution can be coupled to linearly aligned fibers such that the light coupling to each fiber has a small wavelength offset from the neighboring ones. The use of a low-coherence source gives a "spread"-spectral encoding among the fibers for parallel illumination unto the tissue, and it provides several unique characteristics in comparison to the LD-based spectral-encoding approach. First, the wavelength difference in between the neighboring channels is generated by the grating dispersion of a low coherence light, therefore the spectral encoding coupled to the fibers is always reliable and none of the coupled bands will overlap or cross the neighboring ones. This shift-free spectral encoding ensures that none of the data have to be discarded. Second, the interchannel intensity profile always follows the source spectrum, thus the spontaneous channel-to-channel intensity fluctuation can be minimized. This may lead to substantially confined reconstruction uncertainty. Third, the linear fiber bundle used for source coupling can be fabricated with bare or thin-coating fibers, which makes it feasible to arrange the fibers into a circular array inside a small probe for endoscopic interrogation that extends NIR tomography to imaging of internal organs.[18] The implementation of NIR optical tomography to the endoscopic mode was difficult with conventional methods including the LD-based spectral-encoding technique, because the separate coupling of each LD to a connector-terminated fiber or light guide is rather bulky and integrating many channels of such jacketed fibers inside an endoscopic probe is almost prohibitive.

The dimension of the collimated beam strip at the fiber bundle facet plane, as shown in Fig. 1(c), is given by small-angle approximation as

$$L_{\mathrm{FWHM}} = 2f\tan(\Delta\beta) \approx \frac{f\Delta\lambda_{\mathrm{FWHM}}}{p[1-(\lambda_0/p-\sin\alpha)^2]^{1/2}}, \quad (4)$$

where f is the focal length of the collimating lens following the grating dispersion, $\Delta\beta$ is half of the angular dispersion of the low-coherence source by the grating, $\Delta\lambda_{\mathrm{FWHM}}$ is the FWHM spectral bandwidth of the source, λ_0 is the center wavelength of the source, p is the grating period, and α is the beam incident angle with respect to the grating normal. For a linear fiber bundle consisting of N bare fibers aligned side by side, the total spectral band coupled to the fiber bundle is

$$\Delta\lambda_{\mathrm{bundle}} = N\Delta\lambda_{\mathrm{fiber}} = N\frac{d_{\mathrm{fiber}}}{L_{\mathrm{FWHM}}}\Delta\lambda_{\mathrm{FWHM}} = N\frac{d_{\mathrm{fiber}}}{f}p[1-(\lambda_0/p-\sin\alpha)^2]^{1/2}, \quad (5)$$

where $\Delta\lambda_{\mathrm{fiber}}$ is the bandwidth coupled to each fiber, and d_{fiber} is the diameter of one fiber. For this spread-spectral encoding, the argument $\langle\lambda_n\rangle$ of the encoding/decoding operators $\mathbf{\Gamma}(\lambda)$ and $\mathbf{\Gamma}^{-1}(\lambda)$ in Eq. (3) can be replaced by

$$\langle\lambda_n\rangle = \left\langle \lambda_0 + \left(n - \frac{N+1}{2}\right)\Delta\lambda_{\mathrm{fiber}} \right\rangle, \quad (6)$$

where the total number of the bundled fibers N is assumed to be even, and the overall spectral band coupled to the fiber bundle is assumed to be centered at λ_0.

2.3 *Superluminescent Diode: A Low-Coherence Source for Spread-Spectral Encoding*

There are at least three parameters to consider for the use of a low coherence source in spread-spectral encoding: (1) the center wavelength, (2) the spectral bandwidth, and (3) the power. A center wavelength around 800 nm is required as NIR tomography operates in the neighbor of this band. A narrow bandwidth of ~10 nm is preferred for coupling to the fiber bundle to minimize the wavelength-dependent absorption variation that would occur among the source channels. A high power at tens of milliwatts is required to provide sufficient illumination onto each channel following the segmentation of the light power among fibers by spectral encoding. There are a number of types of low-coherence sources available on the market. Among these sources, the light emitting diode (LED) can provide hundreds of milliwatts in a narrow bandwidth of several nanometers, but the collimation and coupling of LED emission into a fiber for grating illumination is rather difficult. A white light source such as a tungsten or halogen lamp provides tens of watts across hundreds of nanometers; however, coupling such a source into small fibers is always highly problematic. A fiber-based stimulated emission amplifier source may provide high power for low-coherence

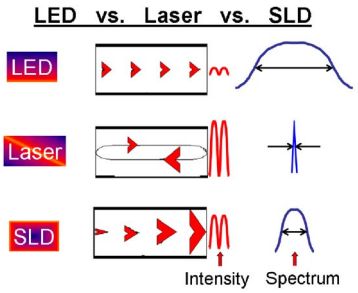

Fig. 2 Comparison of LEDs, LDs, and SLDs, where the SLD produces a medium level of spectral content, as compared to an LED or a laser. The figure is modified from Ref. 21.

light illumination; nevertheless, this type of source is mostly centered around 1300 or 1550 nm. A pulsed light source such as a femtosecond Ti:sapphire laser is perhaps the most powerful within a narrow bandwidth; but this type of source is still currently quite expensive or bulky, although future generations may be more attractive.

A superluminescent diode (SLD) (or superluminescent LED, SLED), is an LED in which there is stimulated emission with amplification but insufficient feedback for oscillations to build up to achieve lasing action.[19] SLDs have similar geometry to LDs, but have no built-in optical feedback mechanism as required by an LD to achieve lasing action for amplification of narrow modes. SLDs have structural features similar to the edge-emitting LED (ELED) that suppresses lasing action by reducing the reflectivity of the facets. A SLD is essentially[20] a combination of an LD and an ELED.

The functioning principles of LEDs, LDs, and SLDs are compared schematically in Fig. 2.[21] An idealized LED emits incoherent spontaneous emission over a wide spectral range into a large solid angle. The unamplified light emerges in one pass from a depth limited by the material absorption. The LED output is unpolarized and increases linearly with input current. An idealized LD emits coherent stimulated emission (and negligible spontaneous emission) over a narrow spectral range and a solid angle. The light emerges after many passes over an extended length with intermediate partial mirror reflections. The LD output is usually polarized and increases abruptly at a threshold current that provides just enough stimulated gain to overcome losses along the round-trip path and at the mirrors. In an idealized SLD, however, the spontaneous emission experiences stimulated gain over an extended path and, possibly, one mirror reflection, but no feedback is provided. The output is low coherence compared with a LD due to the spontaneous emission; on the other hand, it is at high power with respect to an LED because of the stimulated gain. The SLD output, which may be polarized, increases superlinearly versus current with a knee occurring when a significant net positive gain is achieved.[22]

In the last decade, SLDs at several wavelength options have been implemented extensively in low-coherence interferometry[23–28] and optical coherence tomography techniques[29–35] owing to their relatively high power available at the order of 10 mW and a bandwidth of tens of nanometers, which corresponds to a low temporal coherence at an order of 10 μm. The spread-spectral-encoding method presented in this paper demonstrates that SLD sources are also applicable to NIR-DOT.

3 Design and Instrumentation

The schematic structure of the rapid NIR tomography system based on spread-spectral encoding of a SLD source is illustrated in Fig. 3(a), and a photograph of this NIR imager is shown in Fig. 3(b). The SLD (Superlum Inc.) source includes a built-in isolator, and delivers 20-mW fiber-coupled power with an 840-nm center wavelength and a 40-nm FWHM bandwidth. The SLD emission was collimated by an objective lens and directed onto a 1200 grooves/mm diffraction grating. The dispersed light was then collimated by a planoconvex lens of 200 mm focal length. The center portion of the beam strip was coupled to a linear fiber bundle consisting of eight 600-μm bare fibers aligned side by side. The wavelength band of the light coupled to each fiber has a small offset from the neighboring ones, but the coupled bands are adjacent, thus the overall coupling to the fiber bundle forms a "spread-spectral" encoding. The spectrally encoded light was delivered by the linear fiber bundle to a circular imaging array where these fibers split for source illumination. The photograph in Fig. 3(c) illustrates this linear fiber coupling and linear-to-circular delivery configuration. Figure 3(d) details the unfolded top and side views of the beam path from the grating dispersion up to the fiber-bundle coupling. The positioning of the grating center and the linear fiber bundle at the Fourier planes of the collimating lens ensured that the same spectral component of the dispersed beam focused and fell onto the same fiber of the bundle.

The bundled bare fibers were custom-polished and sleeved with black heat-shrinking tubes in between the beam coupler and the imaging array to suppress any crosstalk or ambient lighting background. The diameter of the imaging array was 27 mm, which was identical to that used in the LD-based spectral-encoding system.[16] Thus, the image reconstruction methods used in the LD-based system could be employed, and the system performance could be compared directly. Eight 600-μm-diam detector fibers were interspersed evenly with respect to the source fibers, and these detector fibers were vertically aligned at the spectrometer entrance slit. The spread-spectral-encoded signals were separated vertically by detector fiber location and discriminated horizontally by spectral decoding, such that all S-D pairs were sampled in parallel by a CCD camera.

The spectrometer (Princeton Instruments) had a ruled grating blazed at 1200 lines per mm, which when used in a 300-mm-focal-plane system, provided a spectral spread of 2.7 nm/mm across the detection plane, and measured at a 0.1-nm resolution. A 512×512 CCD camera (Acton Research) having chip size of 8.2×8.2 mm^2 was used to image the spectral spread with flexibility in binning pixels and isolating neighboring channels. The CCD was operated at -30°C, and had a gain control setting up to 4095. This spectrometer-CCD configuration was verified to be able to resolve 10- to 15-nm band spectral-encoded signals.[16] A frame streaming software StreamPix (Norpix Inc.) was used for continuous data acquisition along with real-time frame streaming to the hard disk for off-line image reconstruction. A sampling rate of 5 Hz was achieved at 175 ms of frame ex-

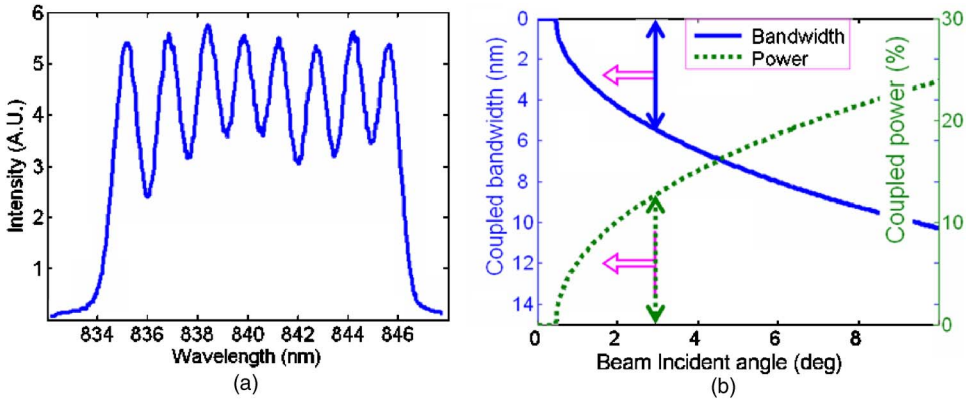

Fig. 4 (a) Spectral profile coupled to the fibers and (b) trade-off between the spectral bandwidth and the power coupling.

posure time, a gain control setting at 3000, and vertical binning of 2 pixels.

4 Characteristics of Spread-Spectral Encoding

4.1 *Spectral Band and Power Coupled into the Linear Fiber Bundle*

The spread-spectral-encoding profile coupled to the linear fiber bundle is plotted in Fig. 4(a). This was measured by placing a detection fiber at the center of the imaging array to form equal distances to all eight sources. The spectral bandwidth coupled to the fibers is $\Delta\lambda_{\text{bundle}}=11.88$ nm, with a near-uniform 1.49-nm increment between neighboring channels. This overall spectral band is slightly wider than that accomplished in the LD-based configuration; however, this band can be reduced by adjusting the dispersion/coupling optics, as illustrated in Eqs. (4) and (5). Because a single source is used, the spectral bandwidth and power coupled to the fibers are associated. This is detailed in Fig. 4(b). Consider a SLD source with a Gaussian spectrum profile of

$$S_0(\lambda)=\frac{2(\ln 2/\pi)^{1/2}}{\Delta\lambda_{\text{FWHM}}}\exp\left[-4\ln 2\left(\frac{\lambda-\lambda_0}{\Delta\lambda_{\text{FWHM}}}\right)^2\right], \quad (7)$$

and assume that only the middle portion of the dispersed beam is coupled to the fiber bundle, the coupled spectrum profile is essentially a Gaussian spectrum truncated on both sides [illustrated in the right half of Fig. 1(c)]. The percentage of the spectrum power remaining in this truncated Gaussian spectrum with respect to the SLD source power is determined by

$$\frac{P_{\text{bundle}}}{P_{\text{source}}}=\text{erf}\left[(\ln 2)^{1/2}\frac{\Delta\lambda_{\text{bundle}}}{\Delta\lambda_{\text{FWHM}}}\right], \quad (8)$$

where erf is the error function defined as

$$\text{erf}(\lambda)=\frac{2}{\sqrt{\pi}}\int_0^{\lambda}\exp(-x^2)\,dx. \quad (9)$$

In Fig. 4(b), the spectral bandwidth and light power coupling into the fiber bundle are calculated versus the beam incident angle on the grating for this SLD-based system. When a bandwidth of 10 nm was coupled to the fiber bundle, the power coupling efficiency was ~24%, and if only 5 nm was coupled to the fiber bundle, the power coupling drops to 10%. This indicated that reducing the bandwidth coupling to further minimize the wavelength-dependent absorption among the sources would cause a major reduction in the total power delivered to the tissue. This, however, can be improved if a source with higher power concentrated at a narrower bandwidth can be employed.

4.2 *Manipulation of the Spread-Spectral-Encoded Data for Image Reconstruction*

The geometry of the 27-mm imaging array is shown in Fig. 5(a), where the eight source positions and eight detector positions are evenly interspersed. For any source, the eight detectors form four sets of distances to the source and vice versa for any detector. The spectral-encoded signals after the spectroscopic separation should then follow the pattern shown in Fig. 5(b), where the size of the white oval indicates the relative strength of the corresponding signal. In this idealized scenario, the spectral band coupled to each fiber is distinctly separated from the neighboring ones even though the fibers are side by side because there are two layers of thin hard cladding in between the neighboring fiber cores (15 μm of cladding for a 600-μm fiber). Thereby, the ovals or the regions of detection (RODs) in Fig. 5(b) do not overlap along the horizontal spectral-encoding direction, and these RODs align in a column along the vertical direction. The actual experimental RODs after the spectral decoding were, however, not clearly differentiated.

The typical spectral-encoding data taken by the CCD are shown in Fig. 5(c), where the gray scale has been compressed to display all low-intensity regions. In Fig. 5(c) the RODs are disguised by horizontal overlapping and vertical offsetting. The vertical offset is due to slight misalignment of the fibers in the fiber adaptor coupled to the spectrometer as well as the astigmatism of the spectrometer. The horizontal overlapping is predominantly due to the finite size of the source beams, the imperfect collimation, and the different S-D distances that make the signals uneven among channels. This horizontal overlapping was nevertheless not a problem in Fig. 4(a) because the spectral encoding was measured for identical S-D distances and the pattern was regular and repeatable.

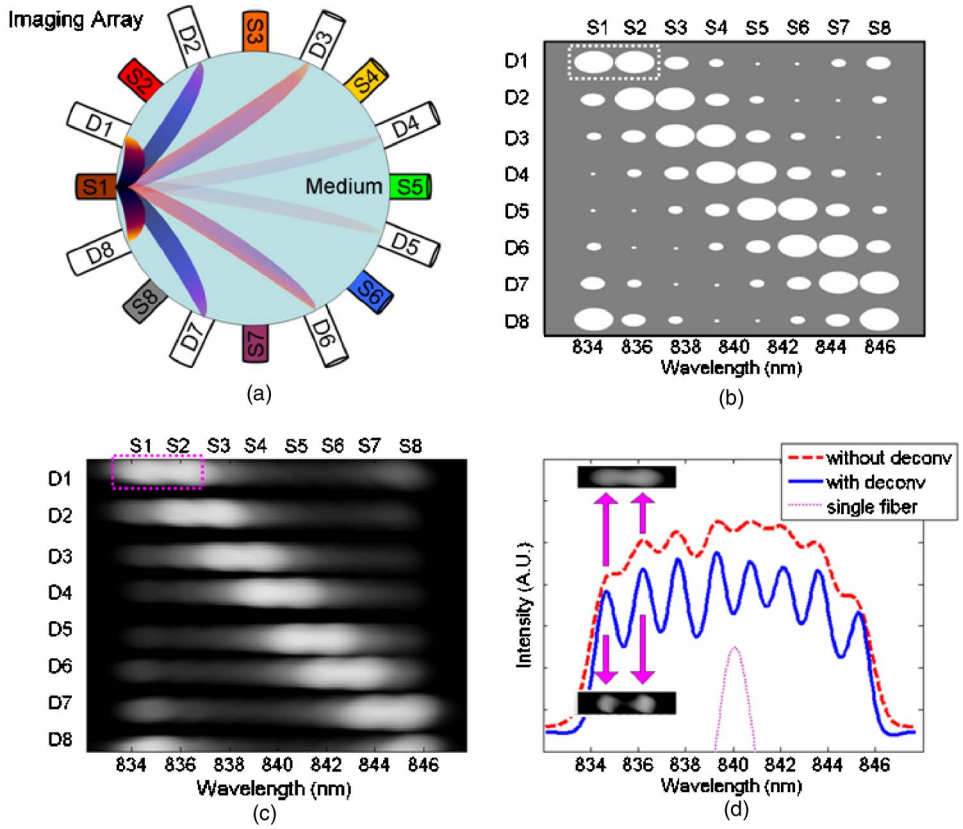

Fig. 5 (a) Imaging array geometry with eight sources (S) and eight detectors (D), (b) an idealized data pattern, (c) the measured data pattern, and (d) the results of deconvolution of the spectrum into individual source contributions shown graphically.

Each ROD must be quantified for data to be fed into the image reconstruction algorithm. Since the spectral-encoding profile is the convolution of a single-fiber-coupling profile with the fiber-configuration function, the individual RODs could be recovered by deconvolving the overlapped profile with a point-spread function corresponding to the single-fiber coupling. The result of this deconvolution to recover RODs is given in Fig. 5(d). The dotted Gaussian shape profile in the middle is the measured single-fiber-coupling profile. The dashed curve is formed by binning the 2-D data in Fig. 5(c) onto the wavelength axis to create a 1-D profile similar to that in Fig. 4(a), and the solid curve is the result of the binning over the data after it has been deconvolved by a measured point-spread function. The spectral separation of eight source channels is clear after the deconvolution, and the identification of two RODs corresponding to the region in the small dashed rectangle in Figs. 5(b) and 5(c) is given as an example in the inset of Fig. 5(d).

4.3 *Shift-Free Encoding and Minimized Reconstruction Uncertainty*

When the 64 RODs were identified after the deconvolution, one intensity data value was averaged for each ROD that accounted for one S-D pair. At this point, the format of the data for image formation was identical to that in the LD-based system, therefore the data calibration and image reconstruction methods used previously could be directly implemented.

The data corresponding to 64 RODs required correction or calibration to compensate for the uneven spectral profile among the source channels and the systematic coupling nonuniformity from the source fiber up to the CCD detector plane. A calibration matrix was introduced for this purpose,[16] which was calculated by fitting the measured S-D signals of a known homogeneous medium versus the S-D distances to the theoretical estimations. The validity of the calibration matrix thus was determined by the stability of the spectral-coupling profile. In the previous LD-based system, the instantaneous wavelength-intensity fluctuation of each channel was independent of the others; therefore the spectral profile used for calculating the calibration matrix was not identical to those used later for image sampling. In this SLD-based system, the spectral encoding was from the single source; thereby the instantaneous intensity change of each coupled channel was always correlated with those of other channels. Moreover, the use of dispersion to create spectral encoding also prevented the coupling profile from wavelength shifting. These two features imply a more stable NIR tomography measurement.

The use of multiple LDs for spectral encoding introduced an average of 1.0 and 1.2% signal intensity fluctuation over 1- and 30-min periods, respectively. The average wavelength shift observed for the LD-based system in a well-controlled situation was 0.027 and 0.21 nm over 1- and 30-min periods, respectively. The long-term wavelength shift over the course of 30 min is greater than the spectrometer resolution of

Table 1 Comparison of the wavelength coupling stability and interchannel intensity fluctuation between the LD-based spectral encoding and SLD-based spread-spectral encoding

	Wavelength Standard Deviation		Intensity Average Fluctuation		μ_a Uncertainty	
	LDs	SLD	LDs	SLD	LDs	SLD
Short term (1 min)	0.027 nm	0.023 nm	1.0%	0.80%	N.A.	1.27%
Long term (30 min)	0.21 nm	0.022 nm	1.2%	0.86%	4.8%	1.49%

0.1 nm, and a 1.2% standard deviation in the intensity fluctuation over this period introduced a 4.8% standard deviation in the reconstructed absorption coefficient value over the time. To evaluate the performance of this SLD-based spread-spectral encoding in terms of wavelength shift and interchannel intensity stability, quantitative measurements similar to those for a LD-based system were conducted.

A 6.35-mm-diam solid phantom rod was positioned at the middle between the center and the inner surface of the imaging array filled by 0.5% Intralipid solution. The solid phantom had an absorption coefficient μ_a of 0.0056 mm^{-1} and a reduced scattering coefficient μ_s' of 1.03 mm^{-1}, which were measured by a frequency-domain NIR tomography system at Dartmouth College. The homogeneous Intralipid background gave μ_a of 0.002 mm^{-1} and reduced scattering coefficient μ_s' of 0.5 mm^{-1}. A total of 300 frames of data were taken for short-term measurement in 1 min at a frame rate of 5 Hz. Similar to the measurement in the LD-based system, a total of 300 frames of data were also taken for long-term measurement of a 30-min period, by simply recording 1 frame for every 30 frames to reduce the data volume. The wavelength stabilities of the eight source channels were measured from the deconvolved curve shown in Fig. 5(d), and the interchannel intensity fluctuation was averaged for all 64 RODs after the deconvolution. Table 1 shows the results, where those for the LD-based system are listed as well for comparison.

The short-term and long-term wavelength shifts of this system were of the order of 0.02 nm, or about 1/5 of the spectrometer resolution. This subresolution shift more likely resulted from the digitization of the signal rather than by the occurrence of actual wavelength shift. Compared with the LD-based system where the long-term wavelength shift was substantially higher than the short-term shift, there is no meaningful difference between the long-term and short-term wavelength shifts in this SLD-based measurement. This validates that the use of a low-coherence source via dispersion provides virtually shift-free spectral encoding among the channels. The interchannel intensity fluctuation of this system was less than, yet close to, that of the LD-based system. The variation of the reconstructed μ_a value in the 300 frames acquired in 30 min is plotted in Fig. 6. Compared with the similar experiments in the LD-based system, the measurement, however, is less clustered, and the uncertainty of the μ_a value was 1.49% standard deviation, a value less than one third of that observed in the LD-based system. Considering that the intensity fluctuation was a perturbation to the image reconstruction, the uncertainty of reconstructed μ_a values appears as an amplification of the data uncertainty. In the LD-based system, the 1.2% perturbation caused a 4 times amplification of 4.8% in the reconstructed absorption coefficient value; whereas in this SLD-based system, the 0.86% perturbation ended up with only 1.49% of uncertainty in reconstruction, an amplification factor less than 2. The significantly reduced amplification of the intensity fluctuation in the SLD-based system implies that the intensity fluctuation in this configuration might be due to the measurement noise rather than any systematic factor, and validates that a more accurate and stable measurement could be made. Both the short-term and long-term stability tests were repeated six times, and similar results were obtained. The relatively small 1.49% reconstruction standard deviation of this 5-Hz rapid NIR tomography system indicated that there was good feasibility of discerning subtle and rapid absorption variations in biological tissues.

5 Results of Imaging Dynamic Objects and Biological Events

5.1 *Imaging Dynamic and Transient Absorption Changes Induced in a Phantom*

Dynamic phantom experiments were conducted to demonstrate the 5-Hz sampling capability of this SLD-based NIR tomography system by use of the same phantom as in Sec. 4.3. In the experiments leading to the images shown in Fig. 7(a), the 6.35-mm-diam phantom rod was moved manually along a circular path inside the 0.5% Intralipid medium, and the manual revolution took slightly less than 2 s. A total of 10 frames were acquired at an interval of 0.2 s, as shown, where

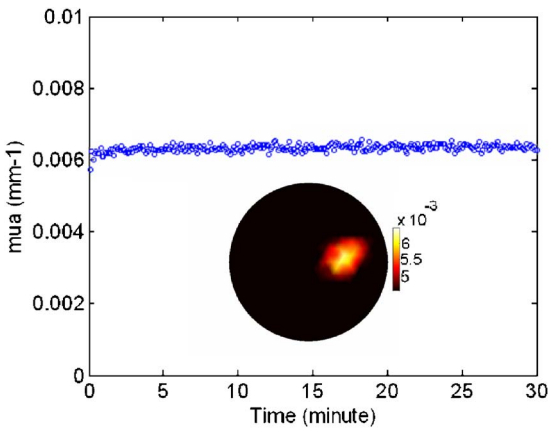

Fig. 6 Stability of the reconstruction over 30 min shown in terms of the absorption coefficient (mua). The plot is the peak value in the cross section of the phantom.

the reconstructed phantom images give a clear course of clockwise movement of the phantom starting from the ~7 o'clock position. The images of the phantom rod are shown as round in all reconstructions except for the ones corresponding to 1.4 and 1.6 s, where the phantom might have been closer to the inner surface of the imaging array.

Another example of dynamic phantom imaging is shown in Fig. 7(b). The 6.35-mm phantom rod was tilted with respect to the normal axis of the imaging array. After the data acquisition started, the phantom was immersed steadily into the Intralipid medium along the inner surface of the imaging array, and then pulled out in a reverse path. The 5-Hz sampling results covering a total of 6 s are displayed, where the time interval between the displayed successive images was 0.6 s. Thus only one of every three frames acquired is displayed for clarity. The image at 0.6 s shows no sign of the occlusion when the lower end of the phantom had not intersected the imaging plane. As the tilted phantom moved down, the sensed cross section of the phantom translated toward the center of the imaging array, and when it passed the array center it moved farther away. When the phantom was pulled back, the sensed phantom cross section followed just the opposite translation path. This is clearly illustrated by the five images in the lower half of Fig. 7(b) that are the opposite of those in the upper half. The results in Figs. 7(a) and 7(b) demonstrate that this SLD-based NIR tomography system is capable of imaging dynamic and transient absorption changes at a 5-Hz sampling rate.

5.2 *Imaging Periodical Absorption Responses Induced by Voluntary Breath-Holding*

The typical resting heart rate (HR) of an adult is between 60 and 100 beats per minute (bpm), therefore the 5-Hz NIR tomography should be sufficient for measuring the absorption changes when induced by normal heart rate pulsation in the capillaries, as is measured by pulse oximetry. An example is given in Fig. 8 to evaluate the feasibility of imaging hemodynamic responses with this system. A male volunteer with a resting HR of 72 bpm was imaged. The volunteer positioned his little finger against the lower-left surface of the imaging array, and practiced voluntary breath-holding starting from when the image acquisition began, to provide a hemoglobin variation signal that was not contaminated by breathing variation and motion artifact. A total of 50 frames were acquired in 10 s. One frame of the reconstructed image is displayed in the upper right of Fig. 8. The cross section of the imaged finger was approximately 13 mm, which corresponds well to the higher absorption area in the image. To assess the time-resolved absorption changes of the finger, the absorption coefficients within 15% difference from the peak value were averaged for each frame. The global absorption changes in 50 frames of acquisition were compared with a simple simulated response by assuming 12 pulsations in 10 s. The simulation curve was placed under the curve of measurement to assess if there was a periodic variation of the responses; thereby the absolute value of the simulated curve is chosen arbitrarily. Note that the variance of the global absorption values follow the simulated periodic pattern quite well, except for the jittering between 1 and 2 s. The mean value of the global absorption coefficient was 0.014 mm^{-1}, which is close to the expected value for human tissue.[36] The variance of the global absorption coefficient at the beginning of the breath-hold was 5.0%, and reduced gradually to 2.9% during the 10 s of breath-holding. Both are above the measured system reconstruction uncertainty of 1.5%.

6 Discussion

The simple *in vivo* study conducted here was chosen to evaluate the system functionality in a well-known setting. The 10-s period for the sampling of hemodynamics in the finger was designed such that from the onset of breath-hold there would not be a detectable change in HR and arterial oxygenation saturation, yet a breath-hold could be used to minimize breathing interference in the signal and motion artifact issues. This current system measures only the absorption at this one wavelength band, and thus does not discriminate oxygenated hemoglobin from deoxygenated hemoglobin. So the absorption is the contribution from both types of hemoglobin as well as other chromophores, such as water and potentially a small contribution from lipid. Although the volunteer managed to keep the finger in position, there is possible slight displacement of the finger that cannot be avoided with *in vivo* studies. It is well known that the sensitivity of DOT close to the boundary and optodes is much higher, and a slight movement away from the array surface may introduce a lower sensitivity measurement to this absorption variance. This effect could account for a reduction in the absorption variance during the 10 s of measurement. If the finger could be obstructively secured for a longer time and a longer voluntary breath-hold beyond 60 to 90 s could be achieved to overcome the oxygen conservation due to the supply of oxygen to the blood from the remaining air in the lungs, noticeable HR reduction could be observed with these longer breath-holds, and a global absorption shift induced by the oxygen saturation change could be identified. Nevertheless, the major objective of this work was more technical than biological, which was to demonstrate that a low-coherence source such as a SLD can be implemented for rapid NIR tomography, and can provide improved system stability. The distinct correlation of the measured global absorption changes with the heart beat has demonstrated the feasibility of hemodynamic imaging by rapid NIR tomography based on this spread-spectral encoding from a low-coherence source such as a SLD.

A frame rate of 5 Hz was achieved in this system, in comparison to the 35 Hz in the LD-based configuration. In spectral encoding, the frame rate is primarily determined by the illuminated light power versus the tissue volume if other imaging parameters are the same. The imaging array, spectrometer, and CCD were almost identical in both systems. In the LD-based setup each of the 8 LDs contributed 10 mW of power to the tissue volume, and a 35-Hz frame rate was obtained by a CCD gain setting at 0; however, in this SLD-based system the single source has only 20 mW of output, and the illumination power of each source channel may be less than 1 mW after the loss by grating dispersion and the splitting among eight fibers. At this low power, the CCD gain had to be set higher and the exposure time had to be set longer to achieve a 5-Hz frame rate capable of imaging hemodynamic changes in tissue. When a smaller tissue volume was imaged, a similar SLD-based setup could lead to higher frame rate.

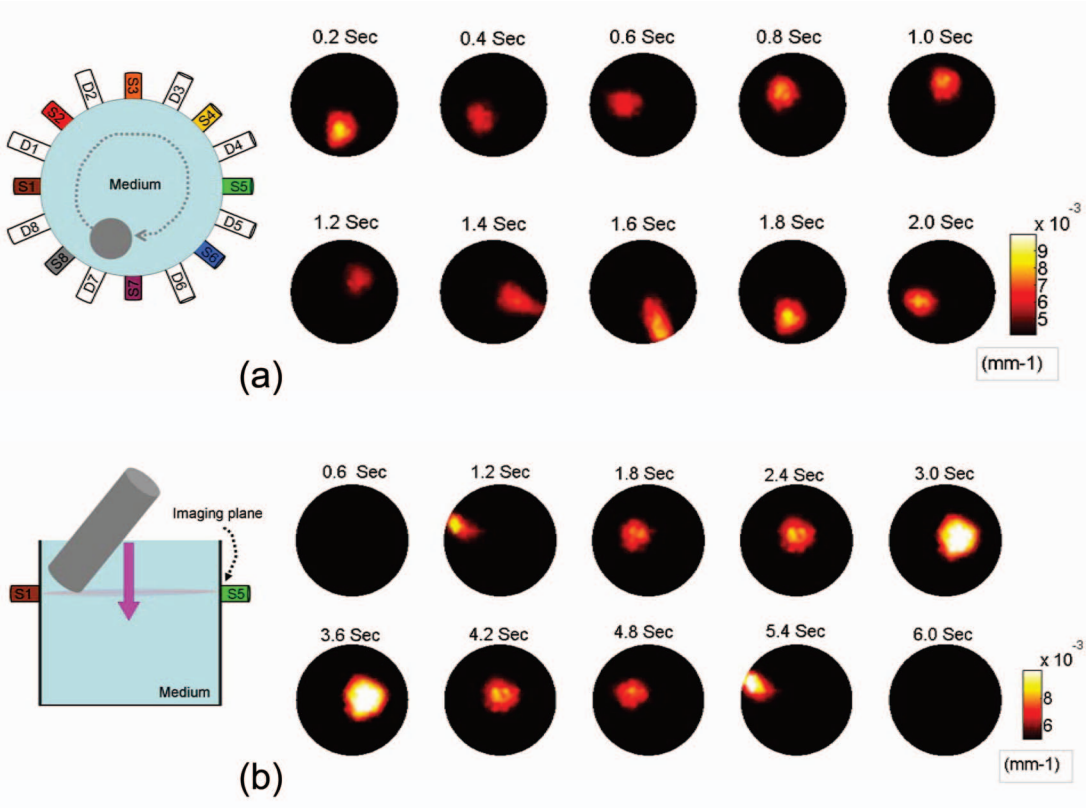

Fig. 7 Imaging of dynamic phantoms is shown with experimental data for (a) a rotating object within a phantom and (b) an object being immersed in the liquid medium of the phantom.

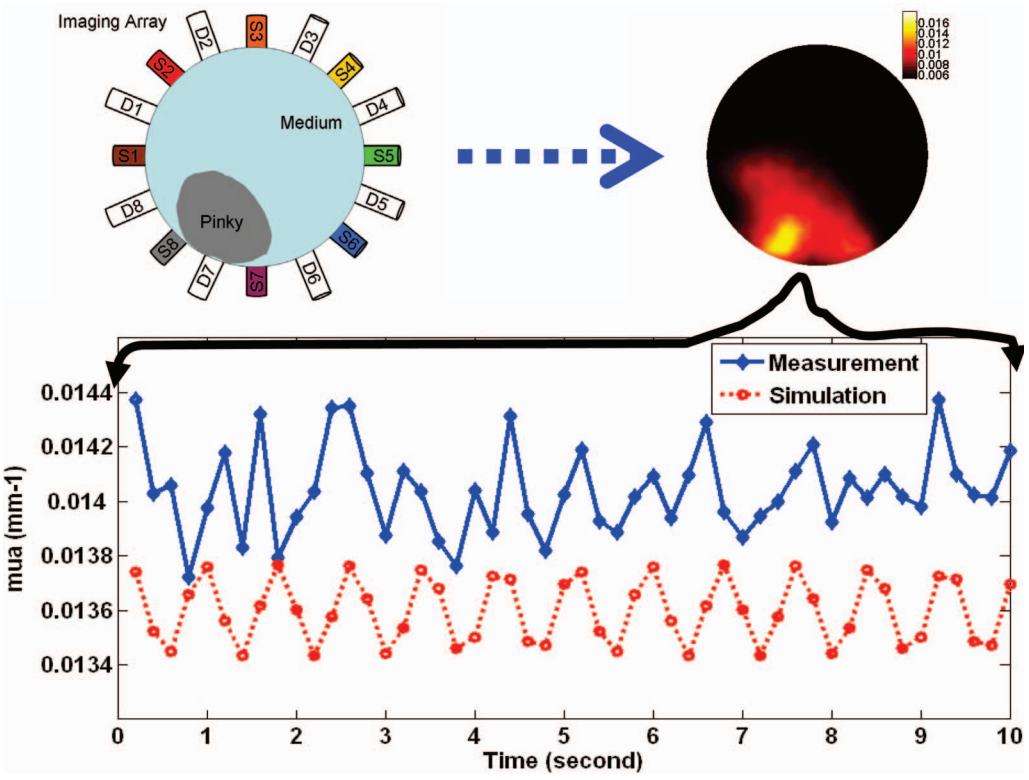

Fig. 8 Imaging of finger during 10 s of breath-holding. The curve shows near-periodic variation of the global absorption value of the finger, and it is correlated to the heart rate of the subject. The global absorption variation is 5.0% at the beginning of the acquisition, and reduces to 2.9% at the end of the 10-s imaging period.

This was confirmed by the 8-Hz frame rate obtained by the endoscopic NIR tomography,[18] where the external tissue volume interrogated by a 12-mm-diam endoscopic NIR probe may be less than the internal tissue volume of this 27-mm imaging array.

Increasing the integrating time of CCD will improve the SNR to account for the weak illumination scenario as in this SLD-based setup; however, this will certainly trade off in the imaging speed. Using CCD is also not desirable if in the future frequency-domain detection is to be implemented to differentiate the absorption and scattering properties of tissue, when in such efforts signal integration time may not be increased. The source power thus sets the ultimate limit of SNR as well as the achievable imaging speed.

The use of spread-spectral encoding from a low-coherence source renders that, in principle, more source fibers can be coupled to improve the image resolution and reconstruction accuracy. Adding on more source fibers, however, will reduce the illumination power of each channel, and therefore higher power density sources will be necessary along with any design that increases the number of source channels, if the sampling speed is to be maintained. The SLD source was utilized in this system for its portability and availability. In terms of the specifications, the source is far from ideal. Only 12 out of 40 nm FWHM was effectively coupled to the fiber, therefore a great portion of the source power was wasted. If the source power were concentrated in the coupled spectral band, a higher imaging speed could have been obtained for the given imaging array, or a larger imaging field of view could be achieved for the same sampling speed. If a more dedicated low-coherence source can be employed, it would be feasible to develop a video-rate imaging speed or apply the system to image larger tissue volumes.

In conclusion, the single SLD-based spectral encoding described here was shown to perform favorably over the LD-based system, in particular the stability and certainty of NIR tomography, except for the frame rate. The data acquisition and processing was sufficient for *in vivo* studies, and the wavelength band used was suitable for hemoglobin-based dynamic studies. Future advancement of this technology may provide a robust means of faster and more accurate measurements of hemodynamics.

Acknowledgments

This work was initially supported by the National Institutes of Health through Grant No. R21CA100984, and has been sponsored by the Oklahoma Center for the Advancement of Science and Technology (OCAST) through a Health Research award HR 06-171.

References

1. B. W. Pogue, S. P. Poplack, T. O. McBride, W. A. Wells, R. S. Osterman, U. L. Osterberg, and K. D. Paulsen, "Quantitative hemoglobin tomography with diffuse near-infrared spectroscopy: pilot results in the breast," *Radiology* **218**(1), 261–266 (2001).
2. B. Chance, Q. Luo, S. Nioka, D. C. Alsop, and J. A. Detre, "Optical investigations of physiology: a study of intrinsic and extrinsic biomedical contrast," *Philos. Trans. R. Soc. London, Ser. B* **352**, 707–716 (1997).
3. M. A. Franceschini, K. T. Moesta, S. Fantini, G. Gaida, E. Gratton, H. Jess, W. W. Mantulin, M. Seeber, P. M. Schlag, and M. Kaschke, "Frequency-domain techniques enhance optical mammography: initial clinical results," *Proc. Natl. Acad. Sci. U.S.A.* **94**(12), 6468–6473 (1997).
4. B. J. Tromberg, O. Coquoz, J. B. Fishkin, T. Pham, E. R. Anderson, J. Butler, M. Cahn, J. D. Gross, V. Venugopalan, and D. Pham, "Noninvasive measurements of breast tissue optical properties using frequency-domain photon migration," *Philos. Trans. R. Soc. London, Ser. B* **352**, 661–668 (1997).
5. Q. Zhu, N. Chen, and S. H. Kurtzman, "Imaging tumor angiogenesis by use of combined near-infrared diffusive light and ultrasound," *Opt. Lett.* **28**(5), 337–339 (2003).
6. Q. Zhang, T. J. Brukilacchio, A. Li, J. J. Stott, T. Chaves, E. Hillman, T. Wu, M. Chorlton, E. Rafferty, R. H. Moore, D. B. Kopans, and D. A. Boas, "Coregistered tomographic x-ray and optical breast imaging: initial results," *J. Biomed. Opt.* **10**(2), 024033 (2005).
7. X. Intes, J. Ripoll, Y. Chen, S. Nioka, A. G. Yodh, and B. Chance, "In vivo continuous-wave optical breast imaging enhanced with indocyanine green," *Med. Phys.* **30**(6), 1039–1047 (2003).
8. V. Ntziachristos, A. G. Yodh, M. D. Schnall, and B. Chance, "MRI-guided diffuse optical spectroscopy of malignant and benign breast lesions," *Neoplasia* **4**(4), 347–354 (2002).
9. A. H. Hielscher, "Optical tomographic imaging of small animals," *Curr. Opin. Biotechnol.* **16**(1), 79–88 (2005).
10. Y. Gu, W. R. Chen, M. Xia, S. W. Jeong, and H. Liu, "Effect of photothermal therapy on breast tumor vascular contents: noninvasive monitoring by near-infrared spectroscopy," *Photochem. Photobiol.* **81**(4), 1002–1009 (2005).
11. Y. Hoshi, I. Oda, Y. Wada, Y. Ito, Y. Yamashita, M. Oda, K. Ohta, Y. Yamada, and M. Tamura, "Visuospatial imagery is a fruitful strategy for the digit span backward task: a study with near-infrared optical tomography," *Brain Res. Cognit. Brain Res.* **9**(3), 339–342 (2000).
12. C. Nolte, M. Kohl, U. Scholz, M. Weih, and A. Villringer, "Characterization of the pulse signal over the human head by near infrared spectroscopy," *Adv. Exp. Med. Biol.* **454**, 115–123 (1998).
13. C. H. Schmitz, M. Löcker, J. M. Lasker, A. H. Hielscher, and R. L. Barbour, "Instrumentation for fast functional optical tomography," *Rev. Sci. Instrum.* **73**(2), 429–439 (2002).
14. C. H. Schmitz, H. L. Graber, Y. Pei, M. Farber, M. Stewart, R. D. Levina, M. B. Levin, Y. Xu, and R. L. Barbour, "Dynamic studies of small animals with a four-color diffuse optical tomography imager," *Rev. Sci. Instrum.* **76**, 094302 (2005).
15. D. Piao, S. Jiang, S. Srinivasan, H. Dehghani, and B. W. Pogue, "Video-rate near-infrared optical tomography using spectrally-encoded parallel light delivery," *Opt. Lett.* **30**, 2593–2595 (2005).
16. D. Piao, H. Dehghani, S. Jiang, S. Srinivasan, and B. W. Pogue, "Instrumentation for video-rate near-infrared diffuse optical tomography," *Rev. Sci. Instrum.* **76**, 124301 (2005).
17. B. W. Pogue, D. Piao, H. Dehghani, and K. D. Paulsen, "Demonstration of video-rate diffuse optical tomography in phantoms and tissues," in *Proc. 2006 IEEE Int. Symp. on Biomedical Imaging*, Arlington, VA (2006).
18. D. Piao, H. Xie, W. Zhang, J. S. Kransinski, G. Zhang, H. Dehghani, and B. W. Pogue, "Endoscopic, rapid near-infrared optical tomography," *Opt. Lett.* **31**(19), 2876–2878 (2006).
19. http://www.its.bldrdoc.gov/fs-1037/dir-035_5184.htm.
20. http://www.tpub.com/neets/tm/110-6.htm.
21. http://www.ee.ucla.edu/~pbmuri/1998-review/simonis/slide6.html.
22. I. P. Kaminow, G. Eisenstein, L. W. Stulz, and A. G. Dentai, "Lateral confinement InGaAsP superluminescent diode at 1.3 μm," *IEEE J. Quantum Electron.* **QE-19**(1), 78–81 (1983).
23. R. C. Youngquist, S. Carr, and D. E. N. Davies, "Optical coherence-domain reflectometry: a new optical evaluation technique," *Opt. Lett.* **12**(3), 158–160 (1987).
24. E. A. Swanson, D. Huang, M. R. Hee, J. G. Fujimoto, C. P. Lin, and C. P. Puliafito, "High-resolution optical coherence domain reflectometry," *Opt. Lett.* **17**(2), 151–153 (1992).
25. H. P. Chiang, W. S. Chang, and J. Wang, "Imaging through random scattering media by using cw broadband interferometry," *Opt. Lett.* **18**(7), 546–548 (1993).
26. X. J. Wang, T. E. Milner, R. P. Dhond, W. V. Sorin, S. A. Newton, and J. S. Nelson, "Characterization of human scalp hairs by optical low-coherence reflectometry," *Opt. Lett.* **20**(6), 524–526 (1995).
27. A. G. Podoleanu, G. M. Dobre, D. J. Webb, and D. A. Jackson, "Simultaneous en-face imaging of two layers in the human retina by low-coherence reflectometry," *Opt. Lett.* **22**(13), 1039–1041 (1997).

28. H. S. Choi, H. F. Taylor, and C. E. Lee, "High-performance fiber-optic temperature sensor using low-coherence interferometry," *Opt. Lett.* **22**(23), 1814–1816 (1997).
29. D. Huang, E. A. Swanson, C. P. Lin, J. S. Schuman, W. G. Stinson, W. Chang, M. R. Hee, T. Flotte, K. Gregory, C. A. Puliafito, and J. G. Fujimoto, "Optical coherence tomography," *Science*, **254**, 1178–1181 (1991).
30. G. J. Tearney, M. E. Brezinski, J. F. Southern, B. E. Bouma, M. R. Hee, and J. G. Fujimoto, "Determination of the refractive index of highly scattering human tissue by optical coherence tomography," *Opt. Lett.* **20**(21), 2258–2260 (1995).
31. J. F. de Boer, T. E. Milner, M. J. C. can Gemert, and J. S. Nelson, "Two-dimensional birefringence imaging in biological tissue by polarization-sensitive optical coherence tomography," *Opt. Lett.* **22**(12), 934–936 (1997).
32. M. J. Everett, K. Schoenenberger, B. W. Colston, Jr., and L. B. Da Silva, "Birefringence characterization of biological tissue by use of optical coherence tomography," *Opt. Lett.* **23**(3), 228–230 (1998).
33. S. Jiao and L. V. Wang, "Two-dimentional depth-resolved Mueller matrix of biological tissue measured with double-beam polarization-sensitive optical coherence tomography," *Opt. Lett.* **27**(2), 101–103 (2002).
34. M. Wojtkowski, A. Kowalczyk, R. Leitgeb, and A. F. Fercher, "Full range complex spectral optical coherence tomography technique in eye imaging," *Opt. Lett.* **27**(16), 1415–1417 (2002).
35. D. Piao, M. Sadeghi, J. Zhang, Y. Chen, A. Sinusas, and Q. Zhu, "A hybrid positron detection and optical coherence tomography system: design, calibration and experimental validation with rabbit atherosclerotic models," *J. Biomed. Opt.* **10**(4), 044010 (2005).
36. W. F. Cheong, S. A. Prahl, and A. J. Welch, "A review of the optical properties of biological tissues," *IEEE J. Quantum Electron.* **26**(12), 2166–2185 (1990).